

Received March 19, 2021, accepted March 26, 2021, date of publication March 30, 2021, date of current version April 8, 2021.

Digital Object Identifier 10.1109/ACCESS.2021.3069712

A Portable Electromagnetic Head Imaging System Using Metamaterial Loaded Compact Directional 3D Antenna

MOHAMMAD SHAHIDUL ISLAM¹, (Graduate Student Member, IEEE),
MOHAMMAD TARIQUL ISLAM¹, (Senior Member, IEEE),
AHASANUL HOQUE¹, (Graduate Student Member, IEEE), MD TARIKUL ISLAM¹,
NOWSHAD AMIN², AND MUHAMMAD E. H. CHOWDHURY³, (Senior Member, IEEE)

¹Department of Electrical, Electronic and Systems Engineering, Faculty of Engineering and Built Environment, Universiti Kebangsaan Malaysia, Bangi 43600, Malaysia

²Institute of Sustainable Energy, Universiti Tenaga Nasional, Kajang 43000, Malaysia

³Department of Electrical Engineering, Qatar University, Doha 2713, Qatar

Corresponding author: Mohammad Tariqul Islam (tariqul@ukm.edu.my)

This work was supported in part by the Universiti Kebangsaan Malaysia, Malaysia, under Grant GUP-2020-017, and in part by the Information and Communication Technology (ICT) Division, Ministry of Posts, Telecommunications and Information Technology, Bangladesh.

ABSTRACT A non-invasive, low-powered, and portable electromagnetic (EM) head imaging system is presented using metamaterial (MTM) loaded compact directional 3D antenna. The antenna consists of two slotted dipole elements with 2×3 and 3×3 finite MTM array elements in top and ground, respectively, and folded parasitic elements that operate within the frequency range of 1.12 GHz to 2.5 GHz. The MTM array elements are optimized to enhance the overall performance regarding antenna bandwidth, realized gain, efficiency, and directionality in both free space and proximity to the head model. The mathematical modelling is also analyzed to justify the integration of MTM unit cells to the top and ground side of the antenna. The impact of MTM on SAR analysis is also performed. A tissue-mimicking 3D head phantom is fabricated and measured to validate the antenna performance. A nine-antenna portable setup is used with the fabricated phantom to measure and collect the scattering parameters that are later analyzed to detect and reconstruct the haemorrhage images by applying the updated IC-CF-DMAS algorithm. The overall performance demonstrates the feasibility of the proposed system as a portable platform to successfully detect, locate and monitor the haemorrhages inside the head in EM imaging system.

INDEX TERMS Metamaterial, 3D antenna, image reconstruction, brain haemorrhage, electromagnetic imaging.

I. INTRODUCTION

Brain injury is a major cause of mortality and disability worldwide, categorized into traumatic and non-traumatic injuries. These injuries often occur by the internal incidences that injure the brain, like tumor and stroke [1]–[4]. The most common brain injury is intracranial haemorrhage (ICH), which refers to blood accumulation inside the human head. It happens due to the bursting of a blood vessel inside the intracranial chamber. The brain injuries deteriorated very rapidly. Thus, fast diagnosis and management are crucial for the treatment and recovery of the injured patient. Therefore,

The associate editor coordinating the review of this manuscript and approving it for publication was Guido Valerio¹.

head imaging is an important factor that can be used for timely medication and on-spot detection to ensure the injured patient's recovery [5]–[7]. CT scan and MRI are the existing susceptible imaging technologies, but they are costly, not easily accessible to the rural areas, and hardly affordable for all patients. The existing imaging systems are very bulky in size, which cannot be easily moveable to any specific place by the pandemic teams for diagnosis purposes. Thus, a compact, non-invasive, non-ionizing, cost-effective, and portable electromagnetic (EM) head imaging system would significantly replace the existing imaging technologies.

EM tomography and wideband EM imaging are the two main approaches that are commonly adopted as EM imaging systems. Wideband EM imaging is a radar-based method that

can localize the significant scatters utilizing the scattering signals over the wide range of microwave frequencies [8], [9]. Nowadays, wideband EM imaging has been widely utilized in breast cancer detection and brain injuries detection [10]–[14]. The main component of the EM head imaging system is the antenna. A low-level EM energy is emitted towards the human head by the antenna array. The scattered signal is then collected and analyzed using different algorithms to reconstruct the interior and localize the injuries inside the human head. The differences in electrical properties between healthy and unhealthy head are applied to detect and reconstruct the images.

As the EM head imaging system consists of multiple combined technologies, the human subject's antenna detection, radiation, and thermal safety are the major concerns [15]. Low-microwave frequencies provide better penetration to the head, but the generated images may have low resolution [16]. That is why attaining a wide bandwidth from 0.5 GHz to 4 GHz can improve image resolution and better penetration capability [17]–[21]. The configuration of the antenna is a major concern as wideband characteristics are demanded with low frequencies. Researchers have been proposing various antennas nowadays for EM head imaging within the lower frequency regimes. A tapered slot antenna is presented at [22] for the EM head imaging. Although the antenna operates within the frequency range of 1GHz to 4GHz, the antenna size is bulky, and it shows low accuracy. A miniaturized T-shaped antenna is presented at [23] for the head imaging, but the antenna can only detect the tumor near the skull due to the very low bandwidth. A grounded coplanar waveguide antenna is presented at [24], where the antenna only shows the simulation analysis with the head model. A triangular patch antenna is presented at [8], where two antenna array elements are used to get the scattering signals that limit the image reconstruction capabilities. A flexible antenna is presented at [25] for the EM head imaging, which only focuses on the scattering parameters and fidelity factor rather than reconstructing the images., the tissue-mimicking phantom is needed for the EM head imaging system to validate the antenna performance. A flexible meander line antenna is presented at [11], where the antenna shows good image reconstruction capabilities. But the overall system's limitation relies upon the homogeneous phantom that does not mimic the real head tissue.

Despite designing and analyzing the conventional antennas, researchers have been introducing the metamaterial (MTM) loaded antennas applicable for EM head imaging systems. The MTM loaded antenna is owing popularity due to the bandwidth enhancement, gain and efficiency enhancement, SAR reduction, and isolation capabilities [26]–[28]. The MTM structures have negative permittivity, permeability, and refractive index parameters that control the EM wave propagation and boost the antenna elements' isolation. Several MTM loaded antennas are presented for the EM imaging systems. A flexible antenna loaded with MTM structure is presented at [29] for human body imaging. The antenna only

focuses on the radiation efficiency and realized gain when placed near the body. There is no image reconstruction analysis presented. An MTM antenna is presented at [30] for the EM head imaging. There is no analysis regarding radiation efficiency, realized gain, and SAR performance when placed near the head model. MTM loaded implantable antenna is presented at [31] for multiple biomedical applications. The analysis relies on the scattering parameters, radiation efficiency, and SAR analysis rather than discussing the application perspective.

This paper presents a portable EM head imaging system with the MTM loaded compact directional 3D antenna. The antenna consists of 2×3 and 3×3 finite hexagonal-shaped MTM arrays on both top and ground sides. The frequency range of the proposed antenna is 1.12 GHz to 2.5 GHz. The transmission line principle is utilized for the mathematical modelling of the proposed MTM loaded 3D antenna. The finite MTM array elements optimize the antenna performance by increasing the bandwidth, realized gain, and efficiency. The MTM structures also enhance radiation efficiency and gain and decrease SAR value when placed near the head model. A tissue-mimicking phantom is fabricated and measured to validate the antenna performance. A nine-antenna setup is used with the fabricated phantom for the portable EM head imaging system to collect the scattered data. The updated Iterative Correction of Coherence Factor Delay-Multiply-and-Sum (IC-CF-DMAS) algorithm is applied to reconstruct and detect the haemorrhage images. The overall performance demonstrates the system's merits as a portable platform and its potential to detect the brain haemorrhages in EM head imaging systems.

II. METAMATERIAL LOADED 3D ANTENNA

The schematic diagrams of the compact directional MTM loaded 3D antenna are given in **Figure 1**. The antenna consists of two PEC side walls, one PEC bottom wall, and one dielectric block. The antenna's top and bottom layers include two top and ground parasitic resonators and finite MTM array structures in both layers. The antenna is printed on the low-cost Rogers RT5880 dielectric substrate where the relative permittivity is 2.2 and loss tangent is 0.0009. The thickness of the substrate and PEC are 1.57 mm and 0.035 mm, respectively. A 2×3 and 3×3 finite hexagonal-shaped MTM arrays are applied to the antenna's top and ground layers. The microstrip feeding is used to the antenna to match the 50Ω impedance. The folded structure with PEC walls is responsible for the antenna directionality. The top and ground layer of the antenna have the same dimensions, which is responsible for the antenna high resonant frequencies. The MTM unit cell structure with effective parameters is depicted in **Figure 2**. Frequency domain-based EM simulator software CST is applied to design and analyze the properties of the unit cell. The MTM unit cell is placed between positive Z-axis and negative Z-axis waveguide ports and energized towards the Z-axis by the electromagnetic wave to get the ideal electromagnetic field distribution. The direction has

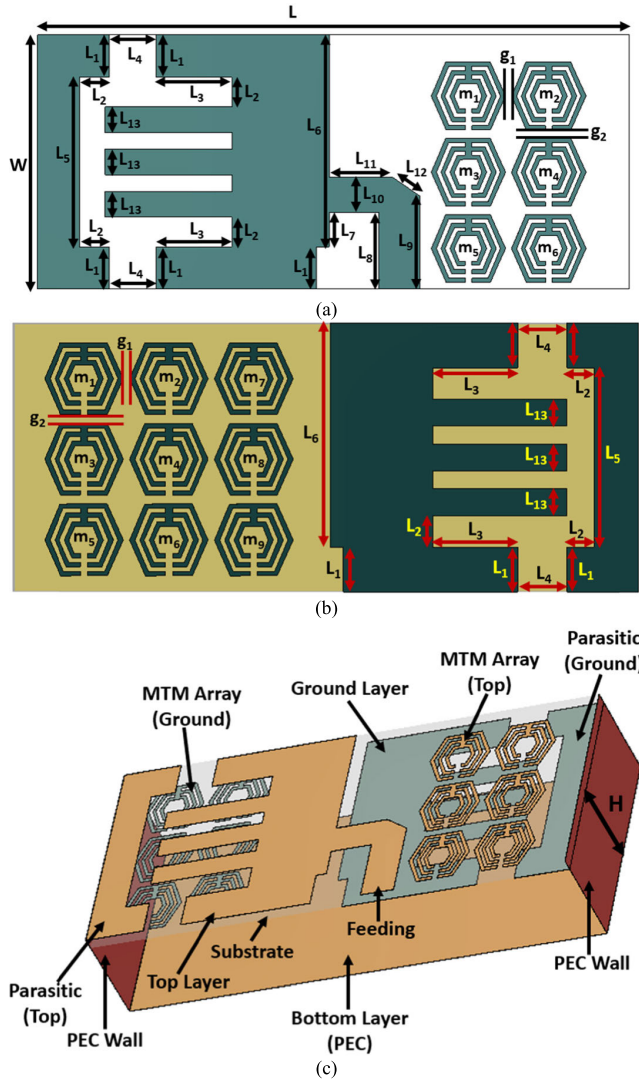


FIGURE 1. Schematics of the proposed antenna (a) Top view (b) Bottom view (c) Perspective view. Dimensions (mm): $L = 70$, $W = 30$, $L_1 = 5$, $L_2 = 3.5$, $L_3 = 9$, $L_4 = 5.5$, $L_5 = 20$, $L_6 = 25$, $L_7 = 4$, $L_8 = 9$, $L_9 = 11$, $L_{10} = 4.2$, $L_{11} = 7.50$, $L_{12} = 3.38$, $L_{13} = 3$, $g_1 = 0.70$, $g_2 = 1.0$.

been set in X-axis and Y-axis for the boundary conditions. Nicolson-Ross-Weir (NRW) method [32] is one of the most popular methods in electromagnetic characterization of the metamaterials used to extract effective medium parameters from the usual incidences of scattering parameter data.

$$\epsilon_r = \frac{2}{jk_0d} \left(\frac{1 - S_{21} + S_{11}}{1 + S_{21} - S_{11}} \right) \quad (1)$$

$$\mu_r = \frac{j2S_{11}}{jk_0d} + \mu_0 \quad (2)$$

$$\eta_r = \frac{2}{jk_0d} \sqrt{\frac{(S_{21} - 1)^2 - S_{11}^2}{(S_{21} + 1)^2 - S_{11}^2}} \quad (3)$$

The frequency range for the proposed MTM structure is 1 GHz to 2.5 GHz. The calculated effective real permittivity and permeability show the positive response within the resonance frequency greater than one. The MTM properties of ($|\epsilon_r| \gg 1$) and ($|\mu_r| \gg 1$) are responsible for improving

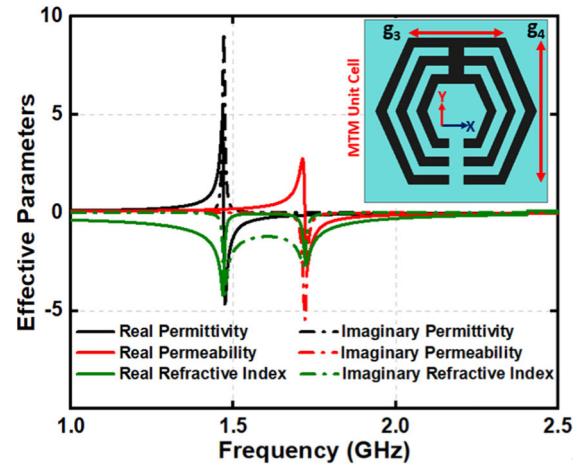


FIGURE 2. Hexagonal-shaped MTM unit cell with effective parameters. Dimensions (mm): $g_3 = 5.3$, $g_4 = 8.0$.

the antenna directivity and realized gain. Equation (4) represents the normalized broadside power when an MTM array element is excited by the wave source that shows the high permittivity's effects in increasing the antenna directivity and gain [33]. Furthermore, the positive permittivity and negative refractive index of the MTM array elements increases the antenna bandwidth by resulting in an additional electromagnetic coupling between the antenna radiating patch and MTM element.

The imaginary parts of the effective parameters are approximately zero from 1 GHz to 1.3 GHz and 1.8 GHz to 2.5 GHz, which indicates the negligible loss of the MTM element.

$$P_N(0) = \frac{K_0^2}{8\pi^2\eta_0\eta_r^2} \quad (4)$$

where,

$$K_0 = \omega\sqrt{\mu_0\epsilon_0} \quad (5)$$

$$\eta_0 = \sqrt{\frac{\mu_0}{\epsilon_0}} \quad (6)$$

$$\eta_r = \sqrt{\frac{\mu_r}{\epsilon_r}} \quad (7)$$

Besides, the miniaturization achieved from the MTM structure increases the electrical length of the antenna elements that impact increasing the antenna bandwidth, efficiency, and realized gain. Moreover, the MTM array elements play a significant role in EM head imaging. The MTM loaded antenna increases the radiation efficiency, realized gain, and directionality when placed near the head model. The MTM array elements can considerably reduce the SAR values, which ensures the electromagnetic radiation safety limit. The evolution of the antenna in free space is depicted in **Figure 3**. The simulated and measured scattering parameters with the simulated evolution are presented in **Figure 3(a)**. The antenna evolution specifies the scattering parameters' changes, which is necessary to optimize the operating frequencies. It is noticeable that the proposed antenna shows the maximum

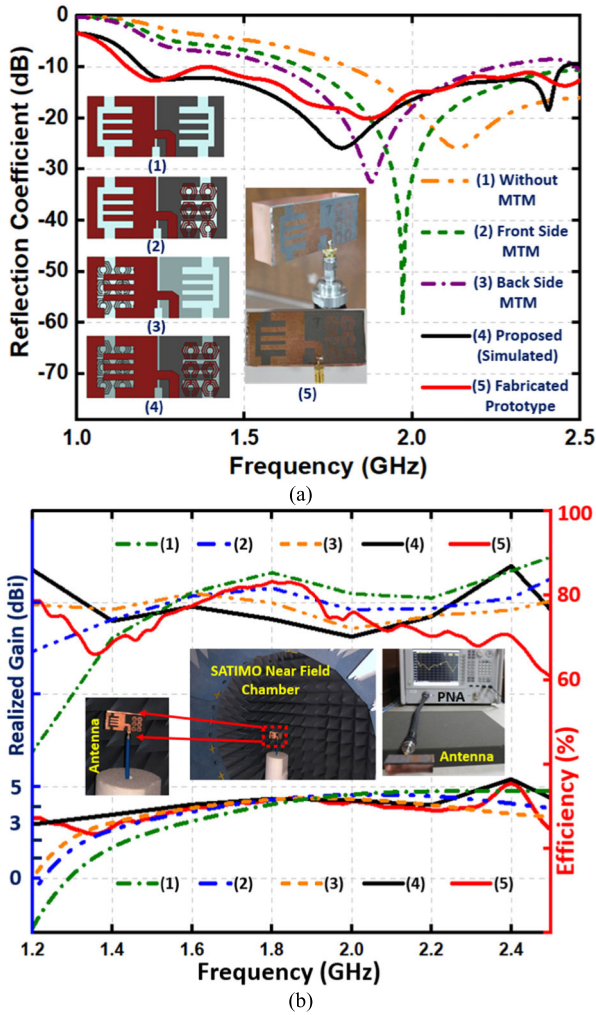


FIGURE 3. Evolution of the antenna with free space measurement (a) Scattering parameters (b) Efficiency and realized gain.

frequency bandwidth compare to the other antennas. The simulated result shows that the proposed antenna operates from 1.17 GHz to 2.47 GHz with a fractional bandwidth of 71.4% for the centre frequency of 1.82 GHz. Moreover, the measurement is performed using Power Network Analyzer (PNA-N5227A), and it shows that the operating frequency is 1.12 GHz to 2.50 GHz with 76.24% fractional bandwidth. The simulated and measured results show good agreement between them. SATIMO near field chamber is used to measure the realized gain, efficiency, and radiation pattern of the proposed fabricated antenna. **Figure 3(b)** shows the realized gain and efficiency of the proposed antenna in simulation with evolution and measurements. The simulated antenna shows the maximum gain of 5.192dBi and 86.8% maximum efficiency within the frequency range of 1GHz to 2.5GHz. The simulated proposed antenna shows the maximum realized gain and efficiency compare to the other antennas. The measurement results show that the maximum realized gain and efficiency are achieved 5dBi and 84%, respectively, which implies a good agreement between the simulated and measured results.

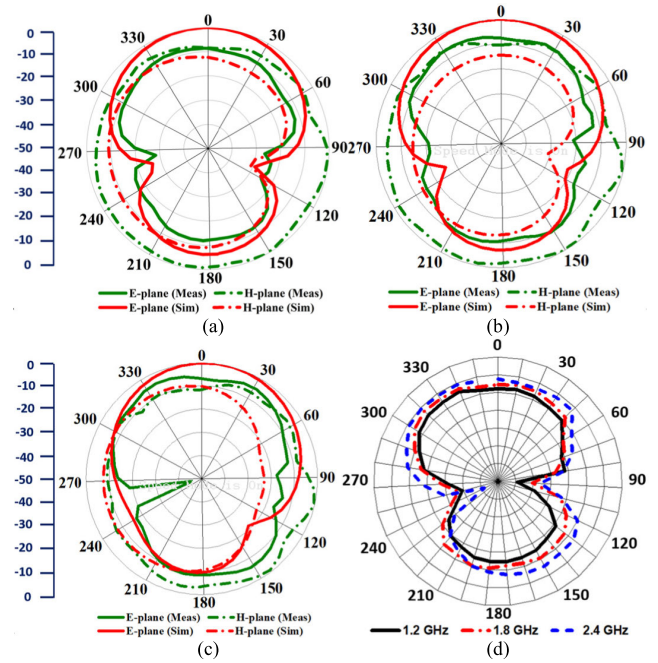


FIGURE 4. E-plane and H-plane radiation pattern (Far-field) at (a) 1.2 GHz (b) 1.8 GHz and (c) 2.4 GHz; (d) E-plane radiation pattern (Near-field) at 1.2 GHz, 1.8 GHz, and 2.4 GHz, respectively.

The simulated and measured E-plane (XZ) and H-plane (YZ) radiation patterns are depicted in **Figure 4 (a-c)** with far-field and near-field radiation characteristics at 1.2 GHz, 1.8 GHz, and 2.4 GHz, respectively. The antenna shows a stable directional radiation characteristic in the stated frequencies with an average gain of 3.8dBi and Z-axis. **Figure 4(d)** presents the antenna near-field measured E-plane characteristics, which also shows a directional characteristic for 1.2 GHz, 1.8 GHz, and 2.4 GHz, respectively. The analysis shows that there is a good match between the simulated and measured radiation characteristics.

The transmission line principle [34]–[36] adopted for equivalent circuit modeling of the proposed metamaterial loaded 3D antenna is depicted in **Figure 5(a)**. Capacitively coupled, two LC tank circuit branches are considered for each plane which represents the main patch architecture. The top and ground plane of patch structures represent a mirror-reflexed arrangement, expecting a change in the number of MTM unit cells. The coupling capacitor equivalences substrate and air gap in the 3D structure. The PEC panels in horizontal and vertical edges are assumed as series LC networks. Besides, each patch structure referred as ‘comb’ in patching resonators is responsible for developing the resonating frequency. The basic patch structure distributed in the top and ground plane shows a mirror symmetry along Y-axis.

$$Z_{in} = Z_0 \frac{Z_L + Z_0 \gamma l}{Z_0 + Z_L \gamma l} \quad (8)$$

Here, the input impedance (Z_{in}) depends on the characteristics impedance (Z_0), length of the line (l), and propagation constant (γ), respectively.

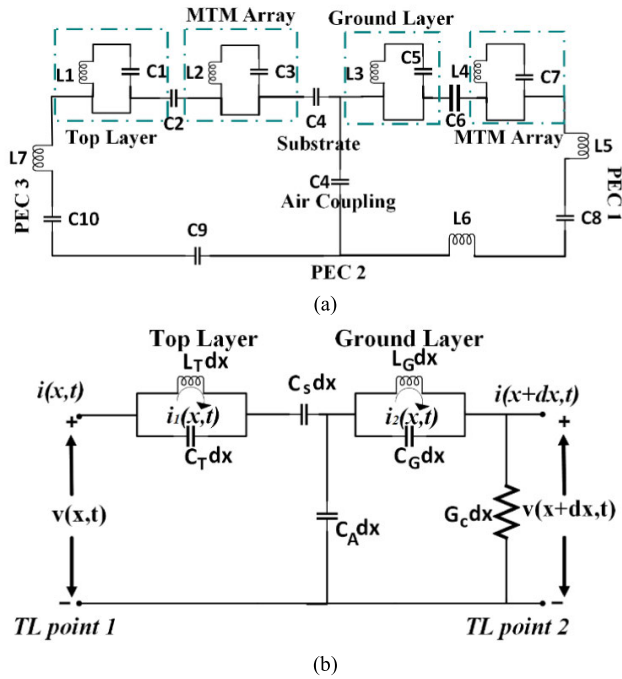


FIGURE 5. (a) Equivalent circuit model for the proposed metamaterial loaded 3D antenna and (b) Simplified equivalent circuit of the proposed metamaterial loaded 3D antenna for mathematical modeling.

Now, the inductance and capacitance (lumped) are considered by the following equations [37], [38].

$$L(nH) = 2 \times 10^{-4} l \left[\ln \left(\frac{l}{w+t} \right) + 1.193 \right. \\ \left. + 0.2235 \frac{w+t}{l} \right] K_g \quad (9)$$

$$C(pF) = \frac{10^{-3} \epsilon_{rd} w l}{36 \pi d} \quad (10)$$

Here, patch width (w), conducting layer thickness (t), and a correction factor (K_g) depend on the three factors such as substrate width and thickness, the dielectric constant of the dielectric film (ϵ_{rd}), and distance between mutual overlapping stripline (d), respectively. Noteworthy to mention that the 3D antenna substrate can be assumed as ‘lossy cavities,’ where an alternative modeling approach, ‘cavity model’ would be further analyzed to approximate more precisely.

For the mathematical modeling of MTM array elements, a simplified equivalent circuit based on lumped element transmission line principle [39] is presented in **Figure 5(b)** for the proposed MTM loaded 3D antenna. Notably, the top layer and ground layer MTM array combination merged with the simplified model. Assume the 3D antenna has two terminal point 1 and 2 with lumped where initial voltage is $v(x, t)$ and initial current is $i(x, t)$, Top layer inductance is $L_T dx$, Ground layer inductance is $L_G dx$, Top layer capacitance is $C_T dx$, Ground layer capacitance is $C_G dx$, substrate effect is $C_s dx$ and 3D structure air gap is $C_A dx$, and conductance on the antenna is $G_c dx$. Besides, Equation (9) and Equation (10) calculate the lumped inductance and capacitance for the numerical approximation of the elements. Reference X-axis

is taken with differential length (dx) and voltage relation between terminal 1 to terminal 2 as follows-

$$V_{lumped}(x, t) = v(x + dx, t) - v(x, t) \\ = -[[-L_T dx] \frac{di_1}{dt} + \frac{1}{C_s} \int i_1 dt \\ + \frac{1}{C_A} \int i_1 dt + [-L_G dx] \frac{di_2}{dt}] \quad (11)$$

Equation (11) represents a general form and takes $dx \rightarrow 0$ with a partial differential equation,

$$\frac{\partial v}{\partial x} = L_T \frac{\partial i_1}{\partial t} - \frac{i_1}{L_T C_T} - \frac{i}{C_s} - \frac{i}{C_A} - L_G \frac{\partial i_2}{\partial t} - \frac{i_2}{L_G C_G} \quad (12)$$

Similarly, the current at terminal 2 is equal to the current at terminal 1 minus the entire current pass through the patch lumped element and conductance at terminal 2. So,

$$\frac{\partial i}{\partial x} = -G_{cv} - i_{1L_T} - i_{1C_T} - i_{2L_G} - i_{2C_G} \quad (13)$$

Simplifying Equation (12-13) by applying the basic circuit solution approach and solving the partial differential equation, One-dimensional form is as below,

$$\left(\frac{1}{G_c L_T} + \frac{1}{G_c L_G} \right) \frac{\partial^2 v}{\partial x^2} = -\frac{C_T}{G_c} \frac{\partial^2 v}{\partial t^2} - \frac{C_G}{G_c} \frac{\partial^2 v}{\partial t^2} - \frac{\partial v}{\partial t} \\ + \frac{v}{L_T L_G G_c} \quad (14)$$

Equation (14) approximation directly addresses the lumped element parameter of the proposed MTM loaded 3D antenna. MTM array incorporation with the compact design is a major key performance enhancer. Therefore, Equation (11) will give a better approximation regarding power consumption or required voltage to estimate the imaging more precisely. This accuracy can be improved by considering surface wave power loss and radiation admittance as a function of tapering strip width following ‘Ricatti equation’ [40]

$$\frac{dY(x)}{dx} + \gamma(x) \left(\frac{1}{Z_c(x)} - Z_c(x) Y^3(x) \right) = 0 \quad (15)$$

where $Z_c(x)$ is the characteristics impedance, and $Y(x)$ is admittance at any arbitrary point x of the transmission line.

III. SENSITIVITY ANALYSIS WITH HEAD MODEL

The sensitivity analysis mostly refers to the antenna scattering parameters on the voxel model with or without tumor, EM-field distribution, and SAR calculation. **Figure 6** represents the scattering parameter of a single antenna that is placed near the head. The analysis shows both simulation and measured scattering parameters. It is noticeable that the scattering parameters that remain below -10dB show a good agreement in both simulation and measurement results. **Figure 7** represents the overall nine antenna setup in top and perspective view with the scattering parameters. Antenna one acts as a transmitter, and the other eight antennas act as receivers. The scattering parameters show that the receiving antennas’ reflection coefficient is below -20 dB and the transmitting antenna has a reflection coefficient of below -10dB.

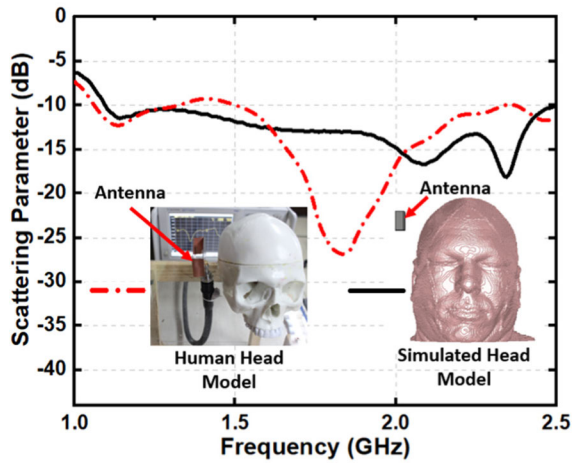


FIGURE 6. Scattering parameters on the simulated and 3D human head model.

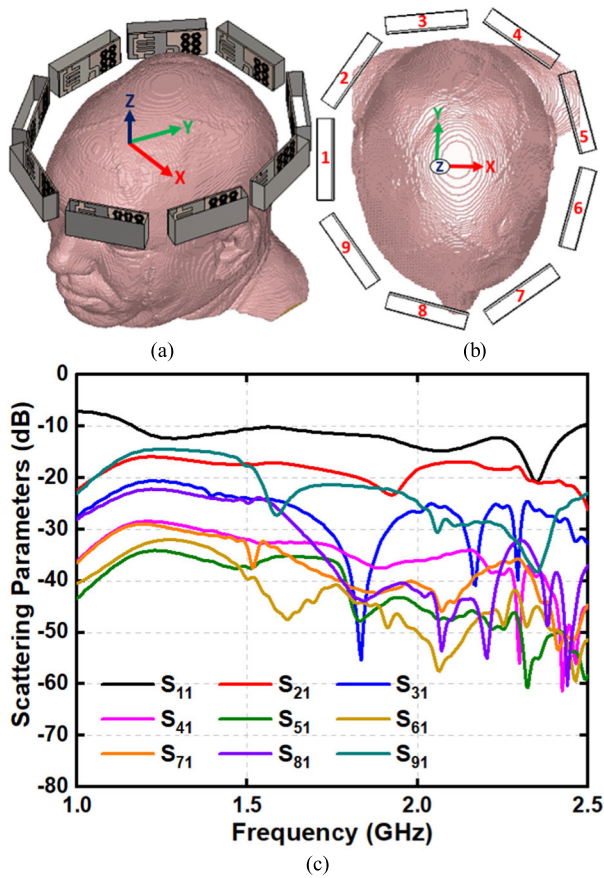


FIGURE 7. Nine antenna system with (a) Perspective view (b) Top View, and (c) Scattering parameters.

The scattering parameters also represent the mutual coupling effects among the antennas, which show a stable performance within 1 GHz to 2.5 GHz. Sample haemorrhages are placed in different locations inside the head model to detect brain injuries. Four different positions are used to analyze the scattering parameter performances with different localized haemorrhages, which is depicted in Figure 8. Figure 8(a) depicts the haemorrhages and antenna positions where they

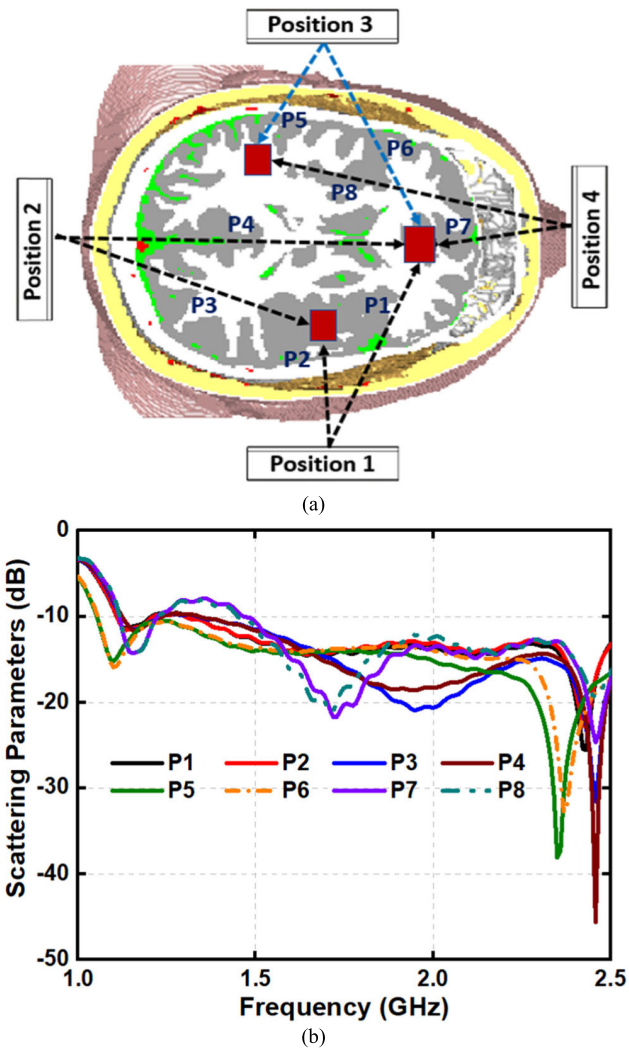


FIGURE 8. (a) Top view with different haemorrhage locations and (b) Scattering parameters.

are marked P1 to P8. Figure 8(b) presents the scattering parameters where one antenna position is considered each time to calculate the result. The results show the scattering performance changes in terms of different localized haemorrhage and antenna positions, and the changes are comparable with the scattering parameters calculated without the haemorrhage placement.

At TEM (1,0) mode, the real and imaginary value of Z_{11} shows a significant effect from MTM in the proposed 3D antenna. Figure 9 shows the Z_{11} performance both in real and imaginary parts during transmission of antenna element 1. The same performance is evaluated for the rest of the antennas (elements 2 to 8). For clarification, the transmission of the first element is considered. A notable performance of impedance optimization using MTM is observed while EM wave propagates from low to the high frequency of the operating range. For the imaginary part, Z_{11} shows (Figure 9(a)) magnitude of 700Ω without MTM, whereas with MTM, the magnitude reduces between 50Ω to 100Ω

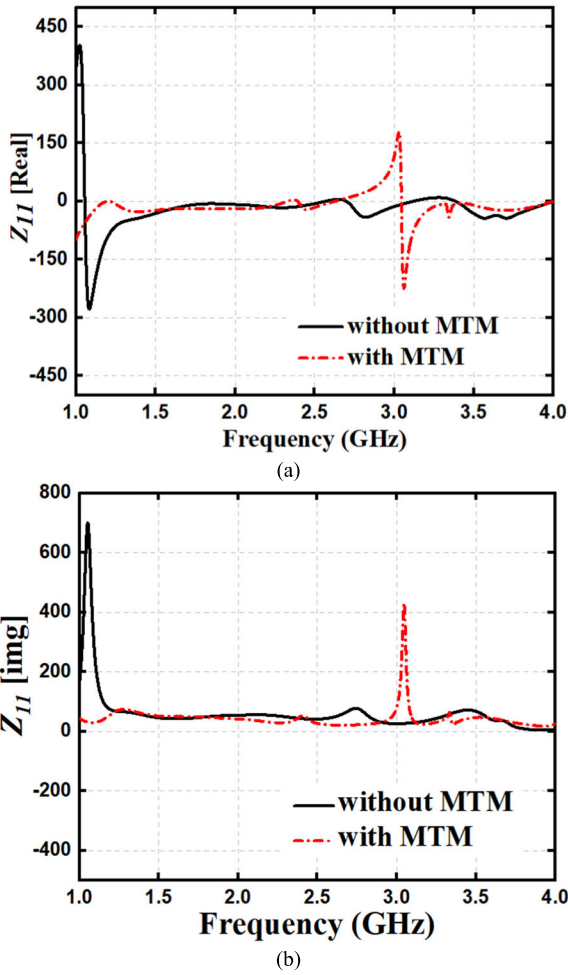


FIGURE 9. Impact of MTM in characteristics impedance during transmission of antenna element 1.

in the entire range except for an unexpected surge at 3GHz. However, the real part of Z_{11} also follows the same pattern since, without MTM, it was 370Ω , and with MTM, it operates within 50Ω . But the sudden increase of Z_{11} (real) at 3GHz still exists. The possible reason for this unexpected behavior could be the anisotropic medium nature of the tissue-mimicking material. The electrical field distribution around the transmitting antenna and phantom is much more dominating; therefore, we get most of the real part of Z_{11} closes to the normalized impedance value. At higher frequency, the dominating nature may be hampered by an anisotropic medium and results in an unexpected magnetic field component. Hence, a sudden impedance change could occur, and precision of tissue-mimicking phantom and better approximation between air dielectric nature around the phantom and transmitting antenna can reduce the effect.

The 3D structure is a combination of coupling and decoupling of patching lines with air as a dielectric medium. Therefore, at any instant, a transmitting antenna with excitation and ports at any location of the imaging setup can be mathematically optimized for impedance calculation. Modified imaging algorithm adopted for the proposed system is not

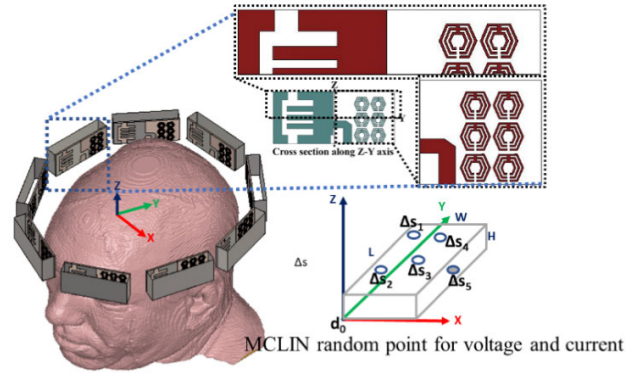


FIGURE 10. Arbitrary voltage and current picking point of antenna element 1 during imaging data extraction.

only introducing MTM for impedance optimization but also affecting the cavity nature of the 3D antenna and ‘Green’s function’ contribution. For example, original Green’s function does not consider the infinitesimal surface current and voltage variation at a random point of any microstrip line [41]. Herein, the rectangular shape is assumed for the 3D antenna shown in Figure 10 considering instantaneous transmitting antenna element and phantom. The 3D dimensional plane is considered similarly as in simulation and antenna length (L), width (W), height (H) for defining any random surface point (Δs) in the microstrip coupled line (MCLIN). Effective permittivity (ϵ_{eff}), air (ϵ_{air}) and substrate (ϵ_s) permittivity, loss tangent ($\tan\delta$) assumed between the antenna and phantom. Random surface points (Δs_1 to Δs_5) are chosen on the MCLIN as the observation point of voltage and current value. In order to distinguish from the original Green’s function and inclusion of precise voltage and current at random MCLIN surface point in the proposed imaging setup, rewrite the function as

$$G_{obs(1..5)} = \frac{1}{LW} \sum_{m=0}^{\infty} \sum_{n=0}^{\infty} (2 - \delta_m)(2 - \delta_n) \times \frac{\epsilon_{eff}\epsilon_{air}\epsilon_s \cos(k_x x)\cos(k_y y)}{k_{mn}^2 - k^2} \quad (16)$$

where $k_{mn}^2 = k_x^2 + k_y^2$, $k_x = (m\pi/L)$, $k_y = (n\pi/W)$ and $m, n = 0, 1, 2, \dots$ i.e. propagation mode considered on the instantaneous transmission. The original functions have been modified by removing permittivity (μ), and 3D antenna height (H) related to higher-order frequency terms since its convergence mechanism makes the overall calculation slow. Now, Equation (16) is incorporated in the algorithm and interpreted or postulated as an alternated solution using coupling and decoupling lines. This approach is beneficial while phantom is surrounded by more than one radiating element or boundaries. If we ignore the boundary, still the EM field arriving at the observation point can be taken as the contribution from the excitation port, and effective dielectric parameters expedite the calculation precision of the proposed imaging system.

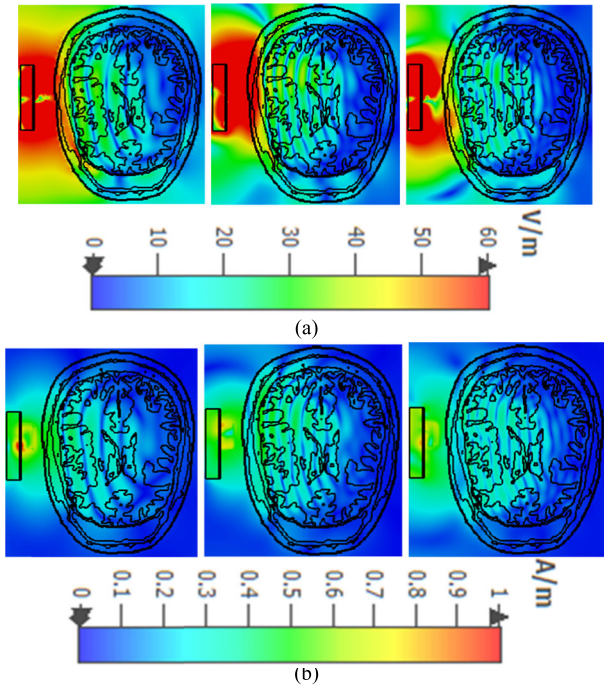


FIGURE 11. (a) E-field and (b) H-field distribution at 1.2 GHz, 1.8 GHz, and 2.5 GHz, respectively from position 1.

Figure 11 represents the E-field and H-field distribution inside the head model at 1.2 GHz, 1.8 GHz, and 2.5 GHz, respectively. The antenna is placed at position 1 to analyze the performances. It is noticeable from the E-field and H-field distribution that the antenna continues to show the directionality to the head model. The nine-antenna setup towards the head model covers the head’s whole area, which conveys all the sufficient information to reconstruct the images.

The antenna’s radiation characteristics in MTM placement near the head model are presented in Figure 12 (a-d). The antenna is placed at position 1 to position 4 with and without the MTM array elements to analyze the antenna directionality at 1.8 GHz and 2.5 GHz, respectively. The proposed MTM loaded antenna shows the maximum directionality compared to the antenna without MTM structure. Besides, the MTM loaded antenna also reduces the back-lobe radiation proximity to the head model. In addition, the antenna cross-polarization behavior, when placed near to the head model at position 3, is depicted in Figure 12 (e). The antenna with MTM and antenna without MTM, both cases have been analyzed at 1.8 GHz to evaluate the cross-polarization behavior of the antenna. It is noticeable that the cross-polarization improves when the MTM is attached to the antenna. However, at some point, the cross-polarization is a bit higher compared to the antenna without an MTM structure. But the cross-polarization value is not high in the direction of high co-polarization. Table 1 charted the effects of the MTM array elements in the realized gain, radiation efficiency, and SAR value are presented, where the antenna is placed near the head model at position 1 to position 4, respectively. The analysis is performed for the resonance frequency of 1.2 GHz,

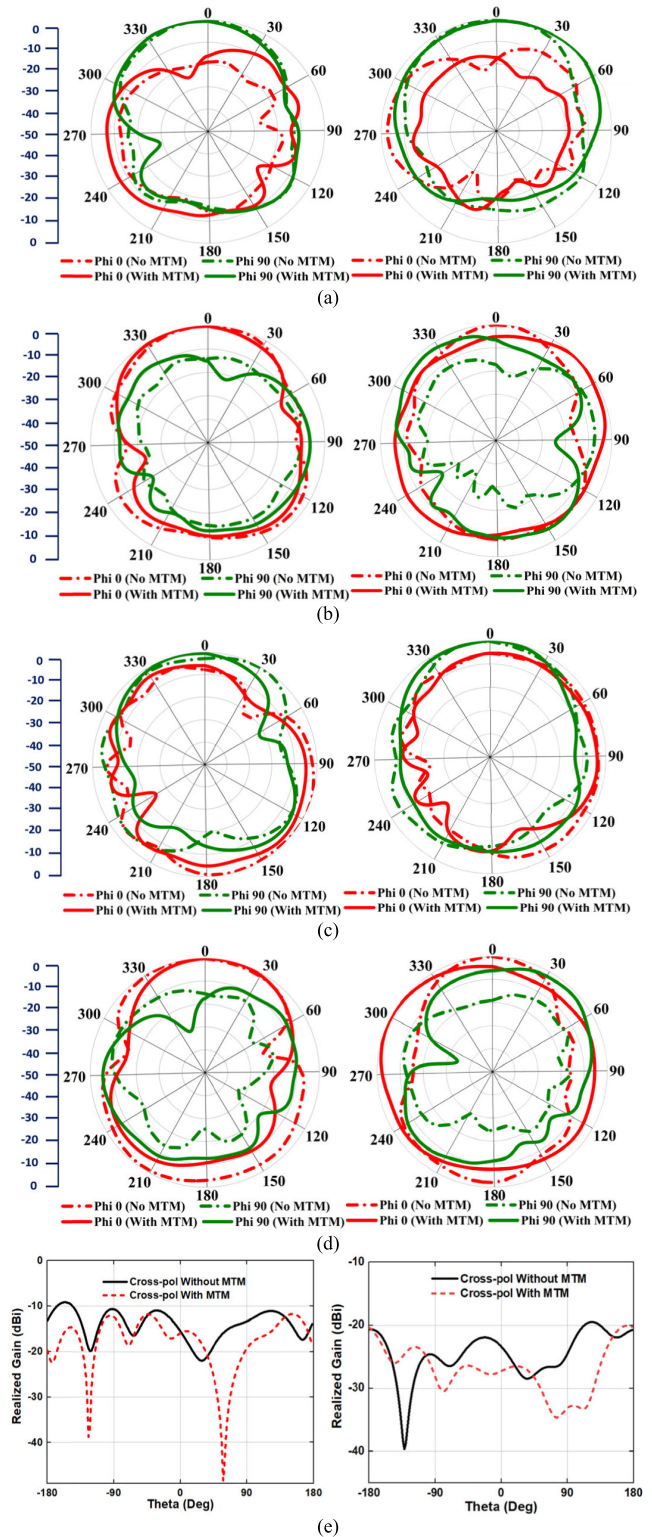
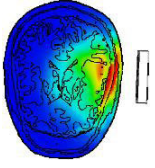
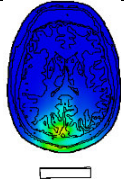
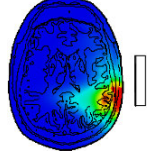
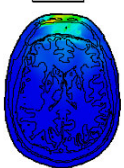


FIGURE 12. Radiation pattern with and without MTM at 1.8 GHz and 2.5 GHz; (a) Position 1 (b) Position 2 (c) Position 3 (d) Position 4 (e) E-plane and H-plane cross-polarization at position 3.

2 GHz, and 2.5 GHz, respectively. It is observing that the radiation efficiency increases when MTM array elements are included with the antenna. The maximum radiation efficiency observed for the antenna without MTM array elements is

TABLE 1. Performance evaluation of the antenna with and without MTM for SAR, radiation efficiency and realized gain.

Antenna Position	Freq. (GHz)	Maximum SAR (W/kg)				Rad. Efficiency (% On Body)		Realized Gain (dB, On Body)	
		Without MTM		With MTM		Without MTM	With MTM	Without MTM	With MTM
		1g	10g	1g	10g				
	1.2	0.013	0.015	0.010	0.008	29	36	-3.17	-1.36
	2	0.044	0.029	0.027	0.018	38	44	0.93	1.25
	2.5	0.038	0.024	0.008	0.006	43	54	1.13	2.75
	1.2	0.029	0.015	0.020	0.009	27	33	-2.80	-1.07
	2	0.071	0.039	0.039	0.021	28	37	-2.21	-0.37
	2.5	0.070	0.034	0.021	0.009	42	47	0.62	1.39
	1.2	0.064	0.015	0.035	0.011	29	49	-5.81	0.43
	2	0.144	0.044	0.105	0.041	18	46	-3.00	1.06
	2.5	0.162	0.063	0.053	0.031	21	49	-1.92	-0.355
	1.2	0.066	0.024	0.025	0.012	28	40	-4.34	-1.23
	2	0.122	0.064	0.112	0.036	25	36	-2.85	-0.89
	2.5	0.189	0.062	0.037	0.013	40	45	-0.36	0.55

43%, where it is 54% for the antenna loaded with MTM array elements. The realized gain also increases when the MTM loaded antenna is placed near the head model. The analysis shows that the maximum realized gain is observed 1.13dBi without the MTM array elements, where it is 2.75dBi for the MTM array elements loaded antenna.

As EM wave radiation is highly harmful to the human body, SAR is an important consideration to ensure operational safety. The following Equation (17) represents the SAR calculation where E and M are electric fields and mass density. σ represents the conductivity of human tissue. As per the standard regulations [42], the maximum SAR must not exceed 2 W/kg for 10g and 1.6 W/kg for 1g of tissue.

$$SAR = \frac{|E|^2 \sigma}{M} \tag{17}$$

The input power of 1mW is used for the 1.2 GHz, 2 GHz, and 2.5 GHz, respectively, in position 1 to position 4. The analysis shows that the maximum SAR value observed is 0.112 W/kg and 0.041 W/kg with the proposed MTM loaded antenna for 1g and 10g of tissue, respectively satisfying the IEEE public radiation exposure limit of 1.6 W/kg. It is noticeable from Table 1 that the SAR value decreases when the MTM array elements are loaded with the antenna. The maximum SAR value for 1g of tissue is 0.189 W/kg without the MTM array elements, where it is 0.112 W/kg for the

TABLE 2. Summary of phantom fabrication recipes.

Components	Dura (500gm)	CSF (500gm)	Gray Matter (500gm)	White Matter (500gm)	Blood (100gm)
Water (gm/ml)	361.90	418.75	403.25	353.35	81.97
Corn flour (gm)	120.65	10.15	82.95	134.30	2.73
Gelatine (gm)	0.00	0.00	0.00	7.05	
Agar (gm)	4.58	56.20	5.2	0.00	12.75
Sodium Azide (gm)	1.8	1.85	1.75	1.75	0.36
Propylene Glycol (gm)	9.65	7.45	4.6	3.55	0.91
Nacl (salt) (gm)	1.20	5.60	2.30	0.00	1.28

proposed antenna. The maximum value without and with MTM array elements observed for 10g of tissue is 0.064 W/kg and 0.041 W/kg.

IV. IMAGE RECONSTRUCTION ALGORITHM

A tissue-mimicking phantom is fabricated and measured to analyze the antenna’s performance and to detect the haemorrhages inside the human head. Dura, CSF, gray matter, white matter, and blood (haemorrhage) are the five elements used to make the tissue-mimicking phantom. The phantom

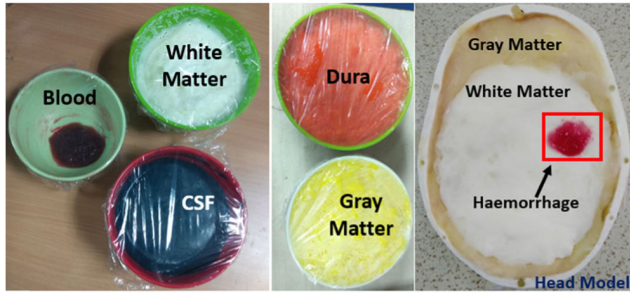
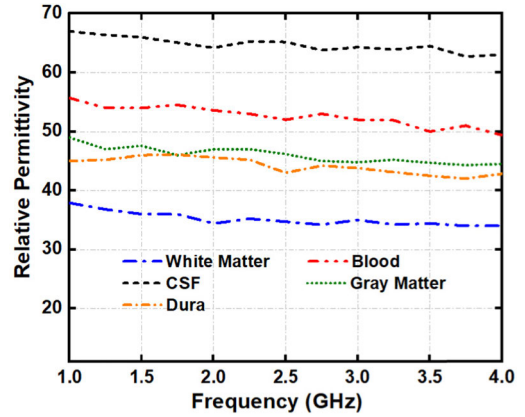


FIGURE 13. Fabricated head phantom components.

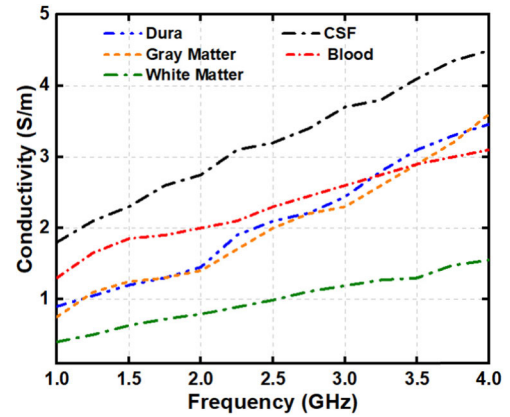
compositions are agar, gelatin, distilled water, cornflour, propylene glycol, sodium azide, and sodium chloride. The summarized recipes are shown in Table 2. After the phantom elements' fabrication, they are placed into the 3D head model to perform the measurement. Figure 13 depicts the overall head phantom components. Dielectric probe kit KEYSIGHT 85070E and power network analyzer (PNA-L N5232A) are used to measure the fabricated phantom materials' electrical properties. The measurement is done over the frequency band of 1GHz to 4GHz. Figure 14 represents the relative permittivity and conductivity of the measured phantom elements. The phantom elements are also measured after one week to check and compare the stability. Significantly less decrement is found between the two measurement results in terms of electrical properties.

Figure 15 represents the proposed EM head imaging system where a nine-antenna array element is used. One antenna acts as a transmitter, and the other eight antennas act as receivers. The system also consists of PNA E8358A transceivers, microcontroller, RF switch, stepper motor, and a portable stand. The tissue-mimicking phantom is placed in the middle of the antenna elements. The PNA is connected with the PC with a GPIB port to post-process the received data to reconstruct the images. The updated IC-CF-DMAS algorithm is used to analyze the microwave signal contrast and reconstruct the images. This IC-CF-DMAS algorithm is an updated version of IC-CF-DAS algorithm that works according to the criteria of phantom imaging [43]. The sample scattered parameters, $S(f, rx, \varphi)$ will be divided into two matrices based on φ where it becomes odd and even, or $S_{odd}(f, rx, \varphi_{odd})$ and $S_{even}(f, rx, \varphi_{even})$, individually, where $\varphi_{odd} = 1, 3, 5, \dots N_\varphi - 1$, and $\varphi_{even} = 2, 4, 6, \dots N_\varphi$. Thus, S_{odd} can be considered initial illumination and S_{even} is the 'offset' illumination. The signals will be translated into time-domain mode applying the Inverse Fourier Transform for generating $\Gamma(t, rx, \varphi_{odd})$. Then, the time domain signals in the $\Gamma(t, rx, \varphi_{odd})$ will be processed using the proposed algorithm to reconstruct the images. The Cartesian 3D coordinates of each point of the imaging domain are contained in the matrix, C , and i display the complete number of points. The coordinates of the transmitter and receiver antenna are A_{Tx} and A_{Rx} , respectively.

The imaging domain is static; hence, the position of the rotating antenna array needs to shift from the reconstruction point. The $P_{Tx\varphi_{odd}-C}$ and $P_{C-Rx\varphi_{odd}}$ are calculated from



(a)



(b)

FIGURE 14. Measured electrical properties (a) Relative permittivity (b) Conductivity.

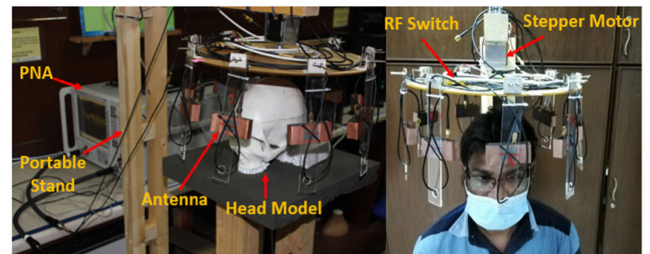


FIGURE 15. Proposed portable EM head imaging system.

C , $A_{Tx\varphi_{odd}}$, and $A_{Rx\varphi_{odd}}$ counting the space between each point and transmitting and receiving antennas. First, the delay is calculated by dividing the total distance l , with the background medium air and the dielectric constant ϵ_r which is presented in Equation (18). c represents the speed of light. The delays are later added to the signal for delivering the proper delayed signal.

$$\tau(i, r_x, \varphi_{odd}) = \frac{\sqrt{\epsilon_r}(PC-Rx\varphi_{odd}(i, r_x, l))}{c} \quad (18)$$

The delayed signals are multiplied and summed to determine the scattering intensity at the regional point of interest shown in Equation (19). The Coherence Factor Delay-Multiply-and-Sum makes use of a weighted sum of the channels where the coherence factor (CF) will become modeled to incentive more coherent channels at every single

stage in the imaging domain with more significant weights. Equation (20-21) presents the steps to calculate scattering map intensity, which is updated by using a weighted sum of channels. After that, the modified delay will be evaluated by the subsequent distance inverse weighting presented in Equation (22-23).

$$\Upsilon_{DMAS}(i) = \int_{-\infty}^{\infty} \sum_{\varphi_{odd}=1} \sum_{rx=1} \left[\Gamma\left(t - \frac{\tau(i, rx, \varphi_{odd})}{\Delta t}, rx, \varphi_{odd}\right) \right] dt \quad (19)$$

$$CF(i) = \frac{\Upsilon_{DMAS}(i)}{\int_{-\infty}^{\infty} \sum_{\varphi_{odd}} \sum_{rx} \Gamma\left(t - \frac{\tau(i, rx, \varphi_{odd})}{\Delta t}, rx, \varphi_{odd}\right) dt} \quad (20)$$

$$\Upsilon_{CF-DMAS}(i) = CF(i) \cdot \Upsilon_{DMAS}(i) \quad (21)$$

$$\Upsilon'(i) = \int_C \frac{\Upsilon_{CF-DMAS}^{n-1}(i)}{1 + p_{C-c}(i, j)} dj \quad (22)$$

$$\tau'(i, rx, \varphi_{odd}) = \tau(i, rx, \varphi_{odd}) + \frac{\Upsilon'(i)}{c} \quad (23)$$

Finally, the scattering strength map will be reconstructed in accordance with the computed coherence factor and modified delays presented in Equation (24-25). These are assessed for $n = 1$ to $n = 7$, and lastly, the convergence is tested by the closure requirements. The iterative process will be prematurely terminated when E_{Υ} decreases to the preferred standard of precision as convergence has pretty much been realized. In this study, $E_{\Upsilon} < 10^{-5}$ will be applied to produce high-quality and noiseless imaging data of an unhealthy phantom that will lead to efficient haemorrhage detection performance.

$$\Upsilon_{CF-DMAS}^n(i) = CF(i) \cdot \Upsilon_{DMAS}^n(i) \quad (24)$$

$$E_{\Upsilon} = \sum \forall i \left| \Upsilon_{CF-DMAS}^n - \Upsilon_{CF-DMAS}^{n-1} \right| \quad (25)$$

The matching medium for the proposed imaging system is optimized by considering the noise and distance of the phantom from the radiating element. So, the background medium is assumed as an Additive White Gaussian Noise (AWGN) channel. The reason behind this assumption supported the Power Spectral Density (PSD) and IC-CF-DMAS algorithm proper delay. Technically, the proposed system hypothetical noise insertion possibility or noise source categorize into three types: Electrical noise, Vibration, and Shot noise. The noise PSD is the square root of the noise power, and the stated noise in this scenario is either left-sided or right-sided PSD. But AWGN considers both-sided spectral power, and a general mathematical model is used to model the timing error as an ideal situation. As we know, for a general AWGN $P_w = N_0 \cdot \frac{F_s}{2}$ where P_w is noise power, N_0 depends on noise power over bandwidth, F_s sampled bandlimited signal

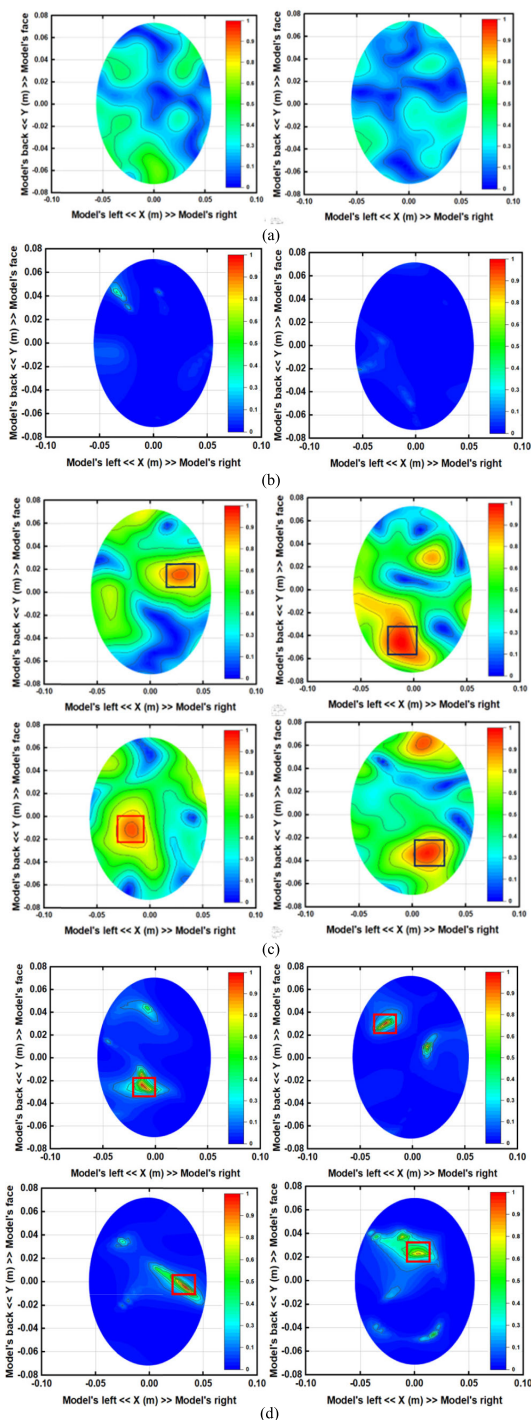


FIGURE 16. Reconstructed images using the proposed antenna on different positions. Blank data using (a) DMAS and (b) IC-CF-DMAS. Human head model with haemorrhage using (c) DMAS and (d) IC-CF-DMAS.

frequency. In other words, Equation (26) is modified as stated in [28]. Here, the matching medium dielectric constant is multiplied with the power of the AWGN channel power.

$$\tau(i, tx, rx, \varphi_{odd}) = \frac{\sqrt{E_{AWGN}} P_w (P_{Tx\varphi_{odd}} - c(i, tx, l) + p_{C-Rx\varphi_{odd}}(i, rx, l))}{c} \quad (26)$$

TABLE 3. Comparison table among the existing EM head imaging antennas with the proposed MTM loaded 3D antenna.

Ref.	Structure	Dim.	Substrate	Substrate layer	MTM inclusion	Fractional Bandwidth (%)	Realized gain (avg.) dBi	FF (%)	Max. SAR (W/kg)	Head Phantom
[20]	3D	80×20×10 mm ³	FR4	2	No	67%	3.15	80		Tissue-mimicking
[42]	3D	68×68×22.5 mm ³	FR4	5	No	51.85%	-	-	0.0147	Inhomogeneous
[44]	3D	70×15×15 mm ³	Rogers RT3000	2	No	97%	3	-		Tissue-mimicking
[45]	3D	25×25×10.5 mm ³	Air	1	No	9.35%	6.6	-		Tissue-mimicking
[46]	3D	70×30×15 mm ³	GIL 1023	2	No	102.2%	<4	-		Tissue-mimicking
[22]	Tapered Slot	95×90×1.28 mm ³	Rogers RO3010	1	No	120%	-	-	-	Tissue-mimicking
[23]	Microstrip	29.99×29.99×0.59 mm ³	FR4	1	No	2.84%	<3	-	0.332	No
[24]	Microstrip	50×44×1.524 mm ³	Rogers RO4350B	1	No	74.3%	<4	98	0.233	No
[8]	Microstrip	79×68.28 mm ²	FR4	1	No	10%	-	-	-	Heterogeneous
This Work	3D	70×30×14	Rogers RT5880	1	Yes	76.24%	>4	80	0.041	Tissue-mimicking

Figure 16 represents the reconstructed images using the DMAS and updated IC-CF-DMAS algorithm. **Figure 16(a-b)** depicts the blank images measured without the placement of the head model inside the system. The observing fact is that the reconstructed images using IC-CF-DMAS show very low noises within the regional area. **Figure 16(c-d)** are the reconstructed images of the head model with haemorrhage identification using DMAS and IC-CF-DMAS algorithms. The rectangular red mark presents the haemorrhage detection and location. Four different haemorrhage locations are used in the head model to examine and evaluate the antenna performance and reconstructed images. The proposed portable system can detect and locate the brain haemorrhage position inside the head model that verifies the system's capability.

V. DISCUSSION

The performance comparison of the proposed MTM loaded 3D antenna with the existing EM head imaging antennas is discussed in this section. **Table 3** is divided into two parts. From [20], [42], [44]–[46], the proposed antenna is compared with the existing 3D antennas and from [8], [22]–[24], it is compared with the other existing antennas. Although some limitations rely into the dimension compare to some of the existing antennas, the proposed MTM loaded 3D antenna shows maximum performance in many features like bandwidth, gain, SAR analysis and tissue-mimicking phantom fabrication.

VI. CONCLUSION

A portable EM head imaging system is presented using the MTM loaded compact directional 3D antenna. 2×3 and

3×3 finite MTM array elements are applied in the top and ground of the 3D antenna. The MTM array elements are optimized to enhance the antenna performance towards the imaging systems. The MTM loaded antenna achieves 5dBi of realized gain and 84% efficiency within the frequency range of 1.12 GHz to 2.5 GHz. The finite MTM array elements also increase the antenna performance when placed near to the head model. They also reduce the SAR during the placement of head proximity. Besides, the antenna shows the stable far-field and near-field directivity performance within the operating band. The proposed EM head imaging system's main components are nine-antenna array elements, tissue-mimicking phantom, PNA, and computing tools to collect and post-process the scattered signals. The validation for the MTM loaded 3D antenna is performed by applying the antenna with the tissue-mimicking phantom. The updated IC-CF-DMAS algorithm is applied to reconstruct the images and locate the haemorrhages, where the reconstructed images indicate that the proposed MTM loaded 3D antenna could be a viable solution in the portable EM head imaging system for the early detection of brain haemorrhages.

REFERENCES

- [1] A. Rajesh, A. M. Daugherty, S. Jain, D. Henry, A. K. Barbey, and R. D. Rubin, "Comorbid conditions differentiate rehabilitation profiles in traumatic versus nontraumatic brain injury: A retrospective analysis using a medical database," *J. Head Trauma Rehabil.*, vol. 35, no. 6, pp. E524–E534, 2020.
- [2] J. Nawabi, A. Morotti, M. Wildgruber, G. Boulouis, H. Kraehling, F. Schlunk, E. Can, H. Kniep, G. Thomalla, M. Psychogios, B. Hamm, J. Fiehler, U. Hanning, and P. Sporns, "Clinical and imaging characteristics in patients with SARS-CoV-2 infection and acute intracranial hemorrhage," *J. Clin. Med.*, vol. 9, no. 8, p. 2543, Aug. 2020.

- [3] M. D. Wheelock, J. P. Culver, and A. T. Eggebrecht, "High-density diffuse optical tomography for imaging human brain function," *Rev. Sci. Instrum.*, vol. 90, no. 5, May 2019, Art. no. 051101.
- [4] F. Khan, I. J. Baguley, and I. D. Cameron, "4: Rehabilitation after traumatic brain injury," *Med. J. Aust.*, vol. 178, no. 6, pp. 290–295, 2003.
- [5] J. J. Heit, M. Iv, and M. Wintermark, "Imaging of intracranial hemorrhage," *J. Stroke*, vol. 19, no. 1, p. 11, 2017.
- [6] G. S. Huang, C. M. Dunham, E. A. Chance, and B. M. Hileman, "Detecting delayed intracranial hemorrhage with repeat head imaging in trauma patients on antithrombotics with no hemorrhage on the initial image: A retrospective chart review and meta-analysis," *Amer. J. Surg.*, vol. 220, no. 1, pp. 55–61, Jul. 2020.
- [7] P. G. Kranz, M. D. Malinzak, and T. J. Amrhein, "Approach to imaging in patients with spontaneous intracranial hemorrhage," *Neuroimag. Clinics North Amer.*, vol. 28, no. 3, pp. 353–374, Aug. 2018.
- [8] B. Sohani, B. Khalesi, N. Ghavami, M. Ghavami, S. Dudley, A. Rahmani, and G. Tiberi, "Detection of haemorrhagic stroke in simulation and realistic 3-D human head phantom using microwave imaging," *Biomed. Signal Process. Control*, vol. 61, Aug. 2020, Art. no. 102001.
- [9] I. Saied and T. Arslan, "Microwave imaging algorithm for detecting brain disorders," in *Proc. 29th Int. Conf. Radioelektronika*, Apr. 2019, pp. 1–5.
- [10] R. Ullah and T. Arslan, "PySpark-based optimization of microwave image reconstruction algorithm for head imaging big data on high-performance computing and Google cloud platform," *Appl. Sci.*, vol. 10, no. 10, p. 3382, May 2020.
- [11] A. S. M. Alqadami, A. E. Stancombe, K. S. Bialkowski, and A. Abbosh, "Flexible meander-line antenna array for wearable electromagnetic head imaging," *IEEE Trans. Antennas Propag.*, early access, Nov. 18, 2020, doi: 10.1109/TAP.2020.3037742.
- [12] M. T. Islam, M. Z. Mahmud, M. T. Islam, S. Kibria, and M. Samsuzzaman, "A low cost and portable microwave imaging system for breast tumor detection using UWB directional antenna array," *Sci. Rep.*, vol. 9, no. 1, Dec. 2019, Art. no. 15491.
- [13] A. Rahman, M. T. Islam, M. J. Singh, S. Kibria, and M. Akhtaruzzaman, "Electromagnetic performances analysis of an ultra-wideband and flexible material antenna in microwave breast imaging: To implement a wearable medical bra," *Sci. Rep.*, vol. 6, no. 1, Dec. 2016, Art. no. 38906.
- [14] A. Salleh, C. Yang, T. Alam, M. Singh, M. Samsuzzaman, and M. Islam, "Development of microwave brain stroke imaging system using multiple antipodal vivaldi antennas based on raspberry Pi technology," *J. Kejuruteran*, vol. 32, pp. 1–6, Feb. 2020.
- [15] A. T. Mobashsher and A. Abbosh, "Development of compact directional antenna utilising plane of symmetry for wideband brain stroke detection systems," *Electron. Lett.*, vol. 50, no. 12, pp. 850–851, Jun. 2014.
- [16] S. Y. Semenov and D. R. Corfield, "Microwave tomography for brain imaging: Feasibility assessment for stroke detection," *Int. J. Antennas Propag.*, vol. 2008, May 2008, Art. no. 254830.
- [17] A. Zamani, A. M. Abbosh, and A. Toaha Mobashsher, "Fast frequency-based multistatic microwave imaging algorithm with application to brain injury detection," *IEEE Trans. Microw. Theory Techn.*, vol. 64, no. 2, pp. 653–662, Feb. 2016.
- [18] H. Bahramiabarghouei, E. Porter, A. Santorelli, B. Gosselin, M. Popovic, and L. A. Rusch, "Flexible 16 antenna array for microwave breast cancer detection," *IEEE Trans. Biomed. Eng.*, vol. 62, no. 10, pp. 2516–2525, Oct. 2015.
- [19] A. T. Mobashsher, K. S. Bialkowski, A. M. Abbosh, and S. Crozier, "Design and experimental evaluation of a non-invasive microwave head imaging system for intracranial haemorrhage detection," *PLoS ONE*, vol. 11, no. 4, Apr. 2016, Art. no. e0152351.
- [20] A. T. Mobashsher and A. M. Abbosh, "Compact 3-D slot-loaded folded dipole antenna with unidirectional radiation and low impulse distortion for head imaging applications," *IEEE Trans. Antennas Propag.*, vol. 64, no. 7, pp. 3245–3250, Jul. 2016.
- [21] M. T. Islam, M. R. I. Faruque, and N. Misran, "Study of specific absorption rate (SAR) in the human head by metamaterial attachment," *IEICE Electron. Exp.*, vol. 7, no. 4, pp. 240–246, 2010.
- [22] B. J. Mohammed, A. M. Abbosh, S. Mustafa, and D. Ireland, "Microwave system for head imaging," *IEEE Trans. Instrum. Meas.*, vol. 63, no. 1, pp. 117–123, Jan. 2014.
- [23] M. S. Bin Nesar, N. Chakma, M. A. Mukhtadir, and A. Biswas, "Design of a miniaturized slotted T-shaped microstrip patch antenna to detect and localize brain tumor," in *Proc. Int. Conf. Innov. Sci., Eng. Technol. (ICISSET)*, Oct. 2018, pp. 157–162.
- [24] A. Hossain, M. T. Islam, M. E. Chowdhury, and M. Samsuzzaman, "A grounded coplanar waveguide-based slotted inverted delta-shaped wideband antenna for microwave head imaging," *IEEE Access*, vol. 8, pp. 185698–185724, 2020.
- [25] A. S. Alqadami, N. Nguyen-Trong, B. Mohammed, A. E. Stancombe, M. T. Heitzmann, and A. Abbosh, "Compact unidirectional conformal antenna based on flexible high-permittivity custom-made substrate for wearable wideband electromagnetic head imaging system," *IEEE Trans. Antennas Propag.*, vol. 68, no. 1, pp. 183–194, Sep. 2019.
- [26] M. Shahidul Islam, M. Samsuzzaman, G. K. Beng, N. Misran, N. Amin, and M. T. Islam, "A gap coupled hexagonal split ring resonator based metamaterial for S-band and X-band microwave applications," *IEEE Access*, vol. 8, pp. 68239–68253, 2020.
- [27] A. F. Almutairi, M. S. Islam, M. Samsuzzaman, M. T. Islam, N. Misran, and M. T. Islam, "A complementary split ring resonator based metamaterial with effective medium ratio for C-band microwave applications," *Results Phys.*, vol. 15, Dec. 2019, Art. no. 102675.
- [28] M. T. Islam, M. Samsuzzaman, S. Kibria, N. Misran, and M. T. Islam, "Metasurface loaded high gain antenna based microwave imaging using iteratively corrected delay multiply and sum algorithm," *Sci. Rep.*, vol. 9, no. 1, Dec. 2019, Art. no. 17317.
- [29] M. Wang, Z. Yang, J. Wu, J. Bao, J. Liu, L. Cai, T. Dang, H. Zheng, and E. Li, "Investigation of SAR reduction using flexible antenna with metamaterial structure in wireless body area network," *IEEE Trans. Antennas Propag.*, vol. 66, no. 6, pp. 3076–3086, Jun. 2018.
- [30] A. S. M. Alqadami, K. S. Bialkowski, A. T. Mobashsher, and A. M. Abbosh, "Wearable electromagnetic head imaging system using flexible wideband antenna array based on polymer technology for brain stroke diagnosis," *IEEE Trans. Biomed. Circuits Syst.*, vol. 13, no. 1, pp. 124–134, Feb. 2019.
- [31] M. Zada, I. A. Shah, and H. Yoo, "Metamaterial-loaded compact high-gain dual-band circularly polarized implantable antenna system for multiple biomedical applications," *IEEE Trans. Antennas Propag.*, vol. 68, no. 2, pp. 1140–1144, Feb. 2020.
- [32] O. Luukkonen, S. I. Maslovski, and S. A. Tretyakov, "A stepwise Nicolson–Ross–Weir-Based material parameter extraction method," *IEEE Antennas Wireless Propag. Lett.*, vol. 10, pp. 1295–1298, 2011.
- [33] S. Ahdi Rezaeieh, M. A. Antoniadis, and A. M. Abbosh, "Bandwidth and directivity enhancement of loop antenna by nonperiodic distribution of mu-negative metamaterial unit cells," *IEEE Trans. Antennas Propag.*, vol. 64, no. 8, pp. 3319–3329, Aug. 2016.
- [34] I. J. Bahl and P. Bhartia, *Microwave Solid State Circuit Design*. Hoboken, NJ, USA: Wiley, 2003.
- [35] I. J. Bahl, "A designer's guide to microstrip line," *Microwaves*, New York, NY, USA, Tech. Rep., 1977, pp. 1–380.
- [36] R. Garg, P. Bhartia, I. J. Bahl, and A. Ittipiboon, *Microstrip Antenna Design Handbook*. Norwood, MA, USA: Artech House, 2001.
- [37] I. Bahl and P. J. N. Y. Bhartia, *Microwave Solid State Circuit Design*. Hoboken, NJ, USA: Wiley, 2003.
- [38] A. Hoque, M. Tariqul Islam, A. Almutairi, T. Alam, M. Jit Singh, and N. Amin, "A polarization independent quasi-TEM Metamaterial absorber for X and Ku band sensing applications," *Sensors*, vol. 18, no. 12, p. 4209, Nov. 2018.
- [39] I. J. Bahl, *Lumped Elements for RF and Microwave Circuits*. Norwood, MA, USA: Artech House, 2003.
- [40] S. Senouci, A. Zerguerras, J. Tao, and T. H. Vuong, "Investigation of an ultra-wideband microstrip antenna using finite elementary lines approach," *Microw. Opt. Technol. Lett.*, vol. 53, no. 12, pp. 2978–2985, Dec. 2011.
- [41] X.-C. Wei, *Modeling and Design of Electromagnetic Compatibility for High-Speed Printed Circuit Boards and Packaging*. Boca Raton, FL, USA: CRC Press, 2017.
- [42] M. Rokunuzzaman, A. Ahmed, T. C. Baum, and W. S. T. Rowe, "Compact 3-D antenna for medical diagnosis of the human head," *IEEE Trans. Antennas Propag.*, vol. 67, no. 8, pp. 5093–5103, Aug. 2019.
- [43] S. Kibria, M. Samsuzzaman, M. T. Islam, M. Z. Mahmud, N. Misran, and M. T. Islam, "Breast phantom imaging using iteratively corrected coherence factor delay and sum," *IEEE Access*, vol. 7, pp. 40822–40832, 2019.
- [44] A. T. Mobashsher, K. S. Bialkowski, and A. M. Abbosh, "Design of compact cross-fed three-dimensional slot-loaded antenna and its application in wideband head imaging system," *IEEE Antennas Wireless Propag. Lett.*, vol. 15, pp. 1856–1860, 2016.
- [45] M. Rokunuzzaman, M. Samsuzzaman, and M. T. Islam, "Unidirectional wideband 3-D antenna for human head-imaging application," *IEEE Antennas Wireless Propag. Lett.*, vol. 16, pp. 169–172, 2017.
- [46] A. T. Mobashsher, A. M. Abbosh, and Y. Wang, "Microwave system to detect traumatic brain injuries using compact unidirectional antenna and wideband transceiver with verification on realistic head phantom," *IEEE Trans. Microw. Theory Techn.*, vol. 62, no. 9, pp. 1826–1836, Sep. 2014.



MOHAMMAD SHAHIDUL ISLAM (Graduate Student Member, IEEE) was born in Bangladesh, in 1993. He received the B.Tech. degree (Hons.) in software engineering from Infrastructure University Kuala Lumpur. He is currently pursuing the M.Sc. degree in electrical and electronic engineering with Universiti Kebangsaan Malaysia (UKM), Malaysia. He is also a Graduate Research Assistant with the Department of Electrical, Electronic, and Systems Engineering, UKM. He is also an ICT

Research Fellow with the Ministry of Posts, Telecommunications and Information Technology, Bangladesh. He has authored or coauthored a number of refereed journals and conference papers. His research interests include the Internet of Things, antenna and wave propagation, wireless communication, and electromagnetic imaging. He was a recipient of the IEEE AP/MTT/EMC Best Paper Award 2019 and 2020.



MOHAMMAD TARIQUL ISLAM (Senior Member, IEEE) is currently a Professor with the Department of Electrical, Electronic and Systems Engineering, Universiti Kebangsaan Malaysia (UKM), and a Visiting Professor with the Kyushu Institute of Technology, Japan. He is the author and coauthor of about 500 research journal articles, nearly 175 conference papers, and a few book chapters on various topics related to antennas, metamaterials, and microwave imaging, with

20 inventory patents filed. Thus far, his publications have been cited 6000 times and his H-index is 38 (Source: Scopus). His Google scholar citation is 8200 and H-index is 42. He has supervised about 30 Ph.D. theses, 20 M.Sc. theses, and has mentored more than ten postdoctoral and visiting scholars. His research interests include communication antenna design, satellite antennas, and microwave imaging. He served as an Executive Committee Member for the IEEE AP/MTT/EMC Malaysia Chapter, from 2018 to 2020. He is also serving as a Chartered Professional Engineer-CEng and a member of IET (U.K.) and a Senior Member of IEICE (Japan). He was a recipient of more than 40 research grants from the Malaysian Ministry of Science, Technology and Innovation, Ministry of Education, UKM Research Grant, and the international research grants from Japan and Saudi Arabia. He received several international gold medal awards, including the Best Invention in Telecommunication Award for his research and innovation, the Publication Award from Malaysian Space Agency in 2009, 2010, 2013, and 2014, the Best Researcher Award from UKM in 2010 and 2011, the Best Innovation Award in 2011, the Best Paper Presentation Award at the International Symposium on Antennas and Propagation (ISAP 2012), Nagoya, Japan, in 2012, the Best Research Group in ICT niche by UKM in 2014, the Best Paper Presentation Award at the IconSpace, Malaysia, in 2015, and the Excellent Award from IEEE AP/MTT/EMC Malaysia Chapter in 2018 and 2019. He was an Associate Editor for *Electronics Letter* (IET). He also serves as a Guest Editor for *Sensors* Journal, an Associate Editor for IEEE ACCESS.



AHASANUL HOQUE (Graduate Student Member, IEEE) received the B.Sc.Eng. degree in electrical and electronic engineering (EEE) from the Chittagong University of Engineering and Technology (CUET), Chittagong, Bangladesh, in 2008, the Master of Science (M.Sc.) degree in electrical engineering from Karlstad University, Sweden, in 2012, with a focus on microwave communication and signal processing, and the Ph.D. degree in electrical and electronics engineering from Uni-

versiti Kebangsaan Malaysia (UKM). He has been an Assistant Professor with the Department of Electrical and Electronic Engineering, International Islamic University Chittagong, Bangladesh, since 2015. He has authored or coauthored a number of refereed journals and conference papers. His research interests include the metamaterial absorber, microwave engineering, wireless communication, solar energy harvesting, and metamaterials.



MD TARIKUL ISLAM was born in Bangladesh, in 1994. He received the B.Sc. degree in computer science and engineering from Patuakhali Science and Technology University (PSTU), in 2016, and the master's degree from the Department of Electrical, Electronic and Systems Engineering, Universiti Kebangsaan Malaysia (UKM), Malaysia, in 2020. He is currently working as a Research Assistant with the Department of Electrical, Electronic and Systems Engineering, UKM. He has

authored or coauthored a number refereed journals and conference papers. His research interests include the communication antenna design, wireless communication, RF engineering, and microwave imaging.



NOWSHAD AMIN is currently serving as a Strategic Hire Professor with the Institute of Sustainable Energy, The National Energy University (@Universiti Tenaga Nasional), Malaysia, and an Adjunct Faculty of engineering and built environment with Universiti Kebangsaan Malaysia (UKM). Earlier, he served over 11 years with the Department of Electrical, Electronic and Systems Engineering, The National University of Malaysia (@Universiti Kebangsaan Malaysia),

from November 2006 to January 2018, where he led the Solar Photovoltaic Research Group, Solar Energy Research Institute (SERI).



MUHAMMAD E. H. CHOWDHURY (Senior Member, IEEE) received the B.Sc. and M.Sc. (Hons.) degrees from the Department of Electrical and Electronics Engineering, University of Dhaka, Bangladesh, and the Ph.D. degree from the University of Nottingham, U.K., in 2014. He worked as a Postdoctoral Research Fellow and a Hermes Fellow with the Sir Peter Mansfield Imaging Centre, University of Nottingham. He is currently working as a full-time Faculty with the Department of

Electrical Engineering, Qatar University. Prior to joining Qatar University, he worked with several universities in Bangladesh. He holds one patent and has published around 60 peer-reviewed journal articles, conference papers, and two book chapters. He is also running several NPRP and UREP grants from QNRF and internal grants from Qatar University, along with academic and government projects. He has been involved in EPSRC, ISIF, and EPSRC-ACC grants, along with different national and international projects. He has worked as a Consultant for the project entitled Driver Distraction Management Using Sensor Data Cloud (2013-2014, Information Society Innovation Fund (ISIF) Asia). His current research interests include biomedical instrumentation, signal processing, wearable sensors, medical image analysis, machine learning, embedded system design, and simultaneous EEG/fMRI. He is also an active member of British Radiology, the Institute of Physics, ISMRM, and HBM. He has received the ISIF Asia Community Choice Award 2013 for the project entitled Design and Development of Precision Agriculture Information System for Bangladesh. He has recently won the COVID-19 Dataset Award for his contribution to fight against COVID-19. He is also serving as an Associate Editor for IEEE ACCESS and a Review Editor for *Frontiers in Neuroscience*.

...